

Latitudinal gradient of spruce forest understory and tundra phenology in Alaska as observed from satellite and ground-based data



Hideki Kobayashi ^{a,*}, Ali P. Yunus ^{a,b}, Shin Nagai ^a, Konosuke Sugiura ^{a,h}, Yongwon Kim ^e, Brie Van Dam ^c, Hirohiko Nagano ^e, Donatella Zona ^{g,i}, Yoshinobu Harazono ^{d,e}, M. Syndonia Bret-Harte ^c, Kazuhito Ichii ^a, Hiroki Ikawa ^e, Hiroki Iwata ^f, Walter C. Oechel ^{g,j}, Masahito Ueyama ^d, Rikie Suzuki ^a

^a Department of Environmental Geochemical Cycle Research, Japan Agency for Marine–Earth Science and Technology, Japan

^b Department of Natural Environmental Studies, The University of Tokyo, Japan

^c Toolik Field Station, Institute of Arctic Biology, University of Alaska, Fairbanks, United States

^d Graduate School of Life and Environmental Sciences, Osaka Prefecture University, Japan

^e International Arctic Research Center, University of Alaska Fairbanks, Alaska, United States

^f Faculty of Science, Shinshu University, Japan

^g Global Change Research Group, San Diego State University, United States

^h Center for Far Eastern Studies, University of Toyama, Japan

ⁱ Department of Animal and Plant Science, University of Sheffield, UK

^j Department of Environment, Earth, and Ecosystems, Open University, Milton Keynes, UK

ARTICLE INFO

Article history:

Received 17 June 2015

Received in revised form 4 February 2016

Accepted 10 February 2016

Available online 23 February 2016

Keywords:

Autumn phenology

Satellite SOS and EOS

Radiative transfer analysis

Alaska

Time-lapse camera

Tundra

Boreal forest

Understory vegetation

ABSTRACT

The latitudinal gradient of the start of the growing season (SOS) and the end of the growing season (EOS) were quantified in Alaska (61°N to 71°N) using satellite-based and ground-based datasets. The Alaskan evergreen needleleaf forests are sparse and the understory vegetation has a substantial impact on the satellite signal. We evaluated SOS and EOS of understory and tundra vegetation using time-lapse camera images. From the comparison of three SOS algorithms for determining SOS from two satellite datasets (SPOT-VEGETATION and Terra-MODIS), we found that the satellite-based SOS timing was consistent with the leaf emergence of the forest understory and tundra vegetation. The ensemble average of SOS over all satellite algorithms can be used as a measure of spring leaf emergence for understory and tundra vegetation. In contrast, the relationship between the ground-based and satellite-based EOSs was not as strong as that of SOS both for boreal forest and tundra sites because of the large biases between those two EOSs (19 to 26 days). The satellite-based EOS was more relevant to snow-fall events than the senescence of understory or tundra. The plant canopy radiative transfer simulation suggested that 84–86% of the NDVI seasonal amplitude could be a reasonable threshold for the EOS determination. The latitudinal gradients of SOS and EOS evaluated by the satellite and ground data were consistent and the satellite-derived SOS and EOS were 3.5 to 5.7 days degree⁻¹ and -2.3 to -2.7 days degree⁻¹, which corresponded to the spring (May) temperature sensitivity of -2.5 to -3.9 days °C⁻¹ in SOS and the autumn (August and September) temperature sensitivity of 3.0 to 4.6 days °C⁻¹ in EOS. This demonstrates the possible impact of phenology in spruce forest understory and tundra ecosystems in response to climate change in the warming Arctic and sub-Arctic regions.

© 2016 The Authors. Published by Elsevier Inc. This is an open access article under the CC BY license (<http://creativecommons.org/licenses/by/4.0/>).

1. Introduction

In the Arctic and sub-Arctic regions, including Alaska, warming trends have been accelerating and the increased trend in surface temperature in the region over the past decade is twofold higher than that in the whole northern hemisphere (Bekryaev, Polyakov, & Alexeev, 2010; Hinzman et al., 2013; IPCC, 2013). It is of particular interest

whether the carbon uptake by terrestrial vegetation increases or decreases due to the change in phenology under climate change (Barichivich et al., 2013; Forkel et al., 2016; Goetz, Bunn, Fiske, & Houghton, 2005; Oechel, Laskowski, Burba, Gioli, & Kalhori, 2014) because the impact of earlier spring onset could be moderated by enhanced ecosystem respiration in the prolonged autumn period (Piao et al., 2008; Ueyama, Iwata, & Harazono, 2014).

Observation and modeling of start of growing season (SOS), end of growing season (EOS), and growing season length provide essential information on how terrestrial vegetation responds to climate changes (Buermann et al., 2014; Keenan et al., 2014; Nagai et al., 2013b; Piao

* Corresponding author at: 3173-25 Showa-machi, Kanazawa-ku, Yokohama, Kanagawa 236-0001, Japan.

E-mail address: hkoba@jamstec.go.jp (H. Kobayashi).

et al., 2011; Richardson et al., 2013b; Schwartz, Ault, & Betancourt, 2013; Verbyla, 2008; Xu et al., 2013). In the Arctic and sub-Arctic regions, the earlier SOS trends were found in previous studies (Buermann et al., 2014; Delbart et al., 2008; Hogda, Tommervik, & Karlsen, 2013; Myneni, Keeling, Tucker, Asrar, & Nemani, 1997; Piao et al., 2011). On the other hand, a relatively limited amount of information is available on large-scale EOS variations and its long-term trends (Jeong & Medvigy, 2014). Recent studies have found a trend for later EOS in many zones in Europe (Garonna et al., 2014), North America (Zhu et al., 2012), and for temperate vegetation over the northern hemisphere (Jeong, Ho, Gim, & Brown, 2011), suggesting that rising temperature could affect the phenological events. However, the environmental factors (e.g. photoperiods and temperature changes) that control the changes in EOS are not clearly understood (Delpierre et al., 2009; Jeong & Medvigy, 2014; Richardson et al., 2013a).

The estimation of SOS and EOS utilizes the seasonal patterns in satellite vegetation indices (VIs). In the Arctic and sub-Arctic regions, an increase in the normalized difference vegetation index (NDVI) (green-up) in spring is partially affected by the timing of snowmelt (Dye & Tucker, 2003; Jonsson, Eklundh, Hellstrom, Barring, & Jonsson, 2010; Kobayashi, Delbart, Suzuki, & Kushida, 2010; Kobayashi, Suzuki, & Kobayashi, 2007; Suzuki, Kobayashi, Delbart, Asanuma, & Hiyama, 2011). A systematic bias has also been found at EOS, and snow is thought to affect the satellite-based EOS estimation (Zhu et al., 2012); however, it has not been investigated quantitatively.

Because boreal forests in Alaska are sparser than forests in lower latitudes (Canada and the U.S.), the seasonality of understory plants has a substantial impact on satellite signals (Pisek & Chen, 2009; Rautiainen & Heiskanen, 2013; Yang, Kobayashi, Suzuki, & Nasahara, 2014). In interior Alaska, black and white spruce are the dominant species. The spectral reflectance of these species with evergreen needles is relatively unchanged throughout the growing season (Nagai et al., 2012), while it is likely that satellite phenology metrics should be greatly influenced by understory plant phenology. However, how the satellite-based phenology metrics are influenced by the forest overstory status, understory plant phenology and other factors such as snow and observation conditions remains less investigated in Alaska. Thus, comparisons with ground-based datasets are essential. Time-lapse camera images provide the seasonal information on surface conditions and have been used widely for the detection of phenological events at ground level (Richardson et al., 2007; Woebbecke, Meyer, Vonbargen, & Mortensen, 1995).

In this study, we quantified the latitudinal gradient of SOS, EOS, and the timing of snow cover in Alaska using ground-based time-lapse digital camera images, and then compared these events with SOS and EOS determined using the satellite data. In the ground-based analysis, we used firsthand time-lapse camera images obtained at 17 sites (six tundra sites and eleven boreal evergreen forest sites) along a latitudinal transect through the state of Alaska, USA (61°N to 71°N), which covers the boreal forest and tundra ecosystems (Fig. 1). We evaluated SOS and EOS by the three phenology algorithms using two satellite datasets (Terra-moderate resolution imaging spectroradiometer (MODIS) and SPOT-VEGETATION). Through the comparison, we investigated the discrepancies in satellite phenology metrics and the influence of snow and understory phenology in tundra and boreal forests. To quantitatively evaluate those impacts, we performed a detailed radiative transfer simulation.

2. Materials and methods

2.1. Study area

The study sites are distributed on a north–south transect across Alaska between a latitudinal range of 61°N to 71°N (Fig. 1). All ground observation sites are within a longitudinal band between 144°W to 157°W. These sites contain two distinct ecosystems: evergreen

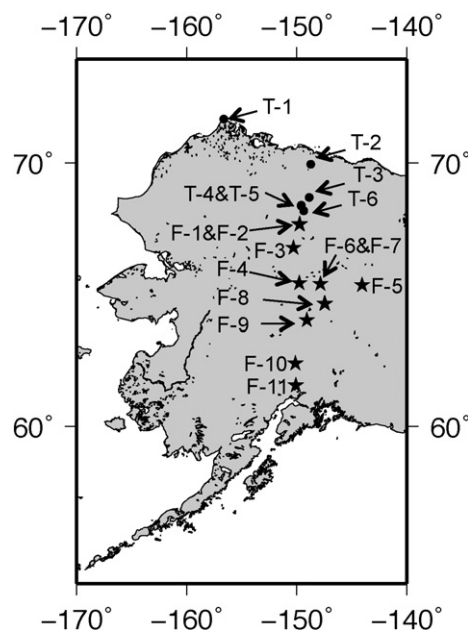


Fig. 1. Geographical distribution of the time-lapse camera locations. Black circles are tundra sites and the stars are forest sites. Full site names are provided in Table 1. Some camera images for individual sites are provided in the supplemental figure.

needleleaf forest and tundra. Evergreen needleleaf forests are found in the south of the Brooks Range (68°N), while the tundra ecosystem is typical of the north. The dominant overstory tree species in interior Alaska is black spruce (*Picea mariana*). Most of the understory layer is covered with rusty peat moss (*Sphagnum fuscum*) and splendid feather moss (*Hylocomium splendens*). The colors of rusty peat moss and splendid feather moss vary spatially and seasonally (brown to green). The understory layer is also partly covered with tussocks formed by herbaceous perennial cotton-grass (*Eriophorum vaginatum*) (Kim, Kodama, Shim, & Kushida, 2014; Nakai et al., 2013). The dominant vascular plants of the understory are low shrubs and herbs such as Labrador tea (*Ledum groenlandicum*), bog bilberry (*Vaccinium uliginosum*), dwarf birch (*Betula nana*), and cloudberry (*Rubus chamaemorus*) (Kim et al., 2014; Nakai et al., 2013). These vascular plants are deciduous. The camera observation sites in the tundra are located in heath tundra and moist acidic tundra areas. The moist acidic tussock tundra is dominated by tussock sedge (*Eriophorum vaginatum*), and dwarf shrubs (*Betula nana*, *Carex bigelowii*, *Vaccinium vitis-idaea*, and *Ledum palustre*) (Euskirchen, Bret-Harte, Scott, Edgar, & Shaver, 2012; Kim et al., 2014; Oechel et al., 2014). The dry heath tundra is dominated by *Dryas* spp., lichen, and dwarf shrubs (Environmental Data Center Team, 2014; Euskirchen et al., 2012).

2.2. Datasets

2.2.1. Time-lapse photography

We used time-lapse camera images obtained from 17 sites across Alaska (Table 1 & Fig. 1). The 6 northern sites (denoted as T-1 to T-6) are located in tundra and the other 11 sites are in boreal forests (denoted as F-1 to F-11). At these sites, there are three different time-lapse camera systems: GardenWatchCams (Brinno Inc., Taiwan), webcams, and a fish-eye camera (Nikon Coolpix 4500 with an FC-E8 fisheye lens) (Table 1). These camera systems took the images of tundra and forest understory vegetation at a nadir or horizontal view. The sampling interval was from 15 min to 6 h depending on the camera setting. Images that were bright enough to obtain color information and in which there were no distinct sunlit or shade variations were selected.

Table 1
Site location, vegetation, and phenology camera system used in this study.

ID	Site	Latitude	Longitude	Camera system	Year	Vegetation type	Reference
T-1	Barrow (BRW)	71.323	−156.626	Webcam	2006	Wet sedge tundra	Zona et al. (2009)
T-2	Coastal tundra (CT)	69.962	−148.726	GardenWatchCam	2011–2013	Wet sedge tundra	Kim (2014)
T-3	Upland tundra (UT)	68.899	−148.867	GardenWatchCam	2011, 2013	Tussock tundra	Kim (2014)
T-4	Brooks range (BRK)	68.626	−149.594	Webcam	2011–2012	Heath tundra	^a
T-5	Toolik lake (TLK)	68.626	−149.594	Webcam	2010, 2012–2013	Moist acidic tundra	^a
T-6	Atigun (ATG)	68.453	−149.367	Webcam	2009–2010	Heath tundra	^a
F-1	Transect-A (T-A)	68.008	−149.736	GardenWatchCam	2011	Understory plants ^b	Sugiura et al. (2013)
F-2	Tundra-boreal forest ecotone (TZ)	67.991	−149.760	GardenWatchCam	2012–2013	Understory plants ^c	Kim (2014)
F-3	Boreal forest at Coldfoot (BC)	67.180	−150.307	GardenWatchCam	2012–2013	Understory plants ^b	Kim (2014)
F-4	Transect-B (T-B)	65.901	−149.764	GardenWatchCam	2011	Understory plants ^b	Sugiura et al. (2013)
F-5	Transect-C (T-C)	65.825	−144.071	GardenWatchCam	2011–2012	Understory plants ^b	Sugiura et al. (2013)
F-6	Poker Flat (PFA)	65.123	−147.487	Fish-eye camera	2012	Black spruce and understory plants	Nagai et al. (2013a, 2013b)
F-7	Poker Flat burnt site (PFAb)	65.117	−147.433	GardenWatchCam	2012	Understory plants ^d	Iwata et al. (2013)
F-8	Univ. Alaska, Fairbanks (UAF)	64.867	−147.850	GardenWatchCam	2011–2013	Understory plants ^b	Ueyama et al. (2014)
F-9	Transect-F (T-F)	64.481	−149.084	GardenWatchCam	2011	Understory plants ^b	Sugiura et al. (2013)
F-10	Transect-H (T-H)	62.746	−150.127	GardenWatchCam	2011	Understory plants ^b	Sugiura et al. (2013)
F-11	Transect-I (T-I)	61.816	−150.089	GardenWatchCam	2011	Understory plants ^b	Sugiura et al. (2013)

^a Environmental Data Center Team (2014).

^b Black spruce forests.

^c White spruce forests.

^d Black spruce burned site.

Areas within images showing tundra or understory vegetation were extracted for analysis.

2.2.2. Installation conditions of time-lapse cameras

T-4, T-5, and T-6 were located near Toolik Lake (Environmental Data Center Team, 2014). The camera system in T-6 (Atigun Gorge) was mounted on a 10 m tower near the Atigun River bridge crossing of the Dalton highway. The two other cameras (T-4 and T-5) were mounted on towers attached to buildings at the Toolik Field Station. The T-5 cameras faced toward Toolik Lake and surrounding shrubs, and the T-4 cameras faced south toward the Brooks Range. The camera images taken at around noon are available publicly (http://toolik.alaska.edu/edc/abiotic_monitoring/image_library.php). The other three tundra sites were located to the north of Toolik Lake. The T-2 and T-3 sites were wet sedge and tussock tundra, respectively. At these sites, GardenWatchCams (Brinno Inc., Taiwan) were installed roughly 1 m above the ground (Kim, 2014). For the T-1 (Barrow) site, images were taken from a web camera installed near the eddy covariance tower in moist acidic tundra (Kwon, Oechel, Zulueta, & Hastings, 2006; Zona et al., 2009). Images were recorded every 15 min from April to September 2006. Data around noontime were used in this study.

The sites F-1 to F-11 were located in black spruce forests in interior Alaska (Iwata et al., 2011; Iwata, Ueyama, Iwama, & Harazono, 2013; Kim, 2014; Nagai et al., 2013a; Sugiura, Nagai, Nakai, & Suzuki, 2013; Ueyama et al., 2014). The F-6 and F-7 sites are close to each other; however, the forest conditions are different: F-6 is a matured black spruce forest and F-7 is a pre-matured black spruce forest after the fire in 2004. Except for F-6, the time-lapse camera images were installed at the forest understory. These time-lapse cameras monitored understory conditions from a nearly horizontal view and any changes in the land surface, such as the snow cover and understory vegetation changes, were easily identified. Images were recorded every 1–4 h throughout the season from 2010 to 2012. However, because these cameras were installed in remote sites under severe climate conditions, there were several large gaps in the data due to technical problems, such as disorientation of the camera by gusts of wind and damaged batteries in cold weather. We selected the years and sites (Table 1) for which understory images provided adequate seasonal coverage. The camera at the F-6 site was a fish-eye camera (Nikon Coolpix 4500 with an FC-E8 fisheye lens) installed at a height of 17 m on the eddy covariance tower of the Ameriflux site (US-Prr) (Ikawa et al., 2015; Nagai

et al., 2013a). The camera faced down and captured an image of the understory surface every hour. The exposure and white balance were set to automatic over the growing season (Nagai et al., 2013a).

2.2.3. Terra-MODIS and SPOT-VEGETATION

Two independent satellite-based surface reflectance datasets, the Terra-MODIS 8-day (MOD09A1) and SPOT-VEGETATION 10-day maximum compositing data (S-10), were used to determine satellite-based SOS and EOS. We collected these satellite datasets for the observation periods of the time-lapse camera: in 2006 and 2010–2013. The MOD09A1 is an atmospherically corrected surface reflectance dataset with a spatial resolution of 500 m (MODIS) (Vermeulen & Vermote, 1999). The SPOT-VEGETATION S10 (1/112 degree) is a 10-day dataset in which the reflectances are calculated by applying the atmospheric correction method of Rahman and Dedieu (1994), which uses fixed values of aerosol optical thickness (AOT). The spectral reflectances in the corresponding locations and observation periods of the time-lapse cameras were extracted. The NDVI and normalized difference infrared index (NDII) (Hardisky, Klemas, & Smart, 1983) were computed from red (RED, 620–670 nm for MODIS and 610–680 nm for VEGETATION), near infrared (NIR, 841–876 nm for MODIS, 780–890 nm for VEGETATION), and shortwave infrared (SWIR, 1628–1652 nm for MODIS and 1580–1750 nm for VEGETATION) reflectances. NDVI and NDII were defined as follows:

$$\text{NDVI} = (\text{NIR} - \text{RED}) / (\text{RED} + \text{NIR}) \quad (1)$$

$$\text{NDII} = (\text{NIR} - \text{SWIR}) / (\text{NIR} + \text{SWIR}). \quad (2)$$

2.2.4. Air temperature data

Monthly 0.5° air temperature data from the Climate Research Unit (Harris, Jones, Osborn, & Lister, 2014) were used to evaluate the latitudinal gradient of air temperature. We extracted the temperature datasets close to the study sites. To compare with phenological events, we used the monthly temperature in May for SOS and an average of August and September in EOS.

2.3. Determination of phenological events

2.3.1. Determination of SOS and EOS

SOS and EOS were determined using time-lapse camera data and satellite datasets. For time-lapse camera data, we first extracted solar

noontime images because they exhibited the best brightness condition. Then we defined the region of interest (ROI) from the images to extract the red, green, and blue digital numbers. The image areas with spruce tree branches and sky were excluded. The true SOS and EOS values were determined by a visual interpretation (D_{SOS_V} and D_{EOS_V}). This was performed for the selected sites (F-1, F-4, F-5, F-7, F-9, F-10, and F-11 in Table 1), where the cameras were installed close to the herbaceous plants and deciduous dwarf shrubs. The dates of D_{SOS_V} and D_{EOS_V} were recorded when the leaf emergence and senescence were recognized clearly in the ROI. This visual interpretation was performed for herbaceous plants and deciduous dwarf shrubs within ROI to exclude seasonal color changes in moss and lichen. In autumn, we determined EOS when all leaves in the ROI were senesced and turned brown.

At sites where it was not possible to conduct a visual interpretation, SOS and EOS were determined from the empirical relationship between phenology metrics derived from a camera-based phenology index (the green excess index [GEI] (Richardson et al., 2007; Woebbecke et al., 1995) and the visually determined SOS and EOS. This empirical relationship was established at sites where visual interpretation was performed (F-1, F-4, F-5, F-7, F-9, F-10, and F-11) and was applied to the rest of the sites (see Section 3.1). The phenology metrics proposed by Zhang et al. (2003) were applied to the GEI. Phenology metrics were derived by the logistic function fitted to the seasonal change in GEIs.

$$GEI_{fit} = \frac{c}{1 + e^{a+bt}} + d \quad (3)$$

where GEI_{fit} and t are a fitted GEI and day of the year, respectively. The a , b , c , and d are site- and season (spring or autumn)-dependent constants for each GEI time series. Two spring (green-up D_1 and maturity D_2) and autumn (senescence D_3 and dormancy D_4) events were then extracted as rate of change in curvature derived from the third order derivative (Fig. 2). The ground-based SOS and EOS were determined based on the empirical relationship between the visually determined D_{SOS_V} and D_{EOS_V} and phenology metrics (D_1 , D_2 , D_3 , and D_4).

For time-series satellite datasets, we applied three algorithms to determine SOS: the local NDVI threshold method (White, Thornton, & Running, 1997), the NDII method (Delbart, Kergoat, Le Toan, Lhermitte, & Picard, 2005), and the method of Zhang et al. (2003). In the local NDVI threshold method, SOS was determined when normalized NDVI exceeded 0.5. In the NDII method, SOS was determined as the point when the NDII in spring reached a minimum value and then increased above a spring threshold. This threshold was determined by the method

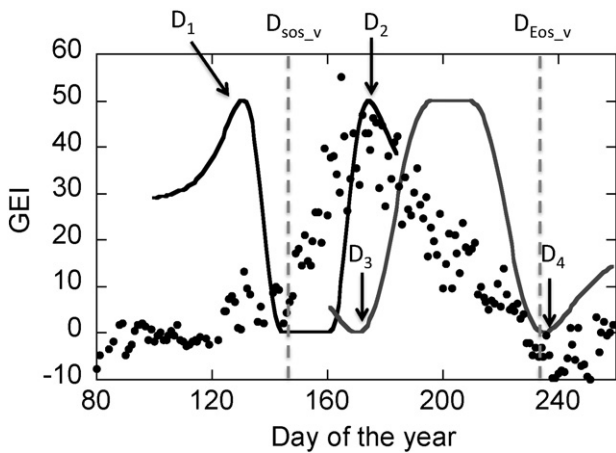


Fig. 2. An example of seasonality in green excess index (GEI), and rate of change in curvatures in spring and autumn periods at the site F-1 in 2011. Gray dotted lines show the SOS and EOS determined visually by the time-lapse camera. D_1 and D_2 are the two spring phenology metrics (green-up D_1 and maturity D_2) derived from the rate of change in curvature, and D_3 and D_4 are the two autumn phenology metrics (senescence D_3 and dormancy D_4) derived in the same manner as D_1 and D_2 .

used in Delbart et al. (2005), which is 20% of the seasonal NDII amplitude. The method of Zhang et al. (2003) was applied to NDVI datasets. Green-up (D_1) and maturity (D_2) were estimated by the fitting method described by Eq. (3). The satellite-based SOS estimate was determined as the midpoint of D_1 and D_2 following a study of reflectance and NDVI seasonality in Siberia (Kobayashi et al., 2007). Fig. 3 shows examples of the seasonal variations in NDVI, NDII and GEI. For autumn timings, the local NDVI threshold method was used to determine EOS. The method of Zhang et al. (2003) should be theoretically applicable in the same manner as for SOS. However, in our study area, the temporal patterns of NDVI in autumn were complex due to multiple occurrences of snowfall and snowmelt until the ground was covered with lingering snow. Thus the NDVI fitting using the logistic function frequently failed.

The errors of three satellite-based methods from two satellite datasets were evaluated using two statistical metrics (mean bias and root mean square error (RMSE)). The mean biases were computed by:

$$Mean\ bias = \frac{1}{N} \sum_{i=1}^N (X_{g,i} - X_{sat,i}) \quad (4)$$

where $X_{g,i}$ and $X_{sat,i}$ are either SOS or EOS obtained from the time-lapse camera and satellite for the i th estimated cases. Positive bias indicates that the satellite-based estimates of SOS or EOS tend to be earlier than the ground-based estimates. The RMSE was computed by:

$$RMSE = \sqrt{\frac{1}{N} \sum_{i=1}^N (X_{g,i} - X_{sat,i})^2} \quad (5)$$

The estimated SOS and EOS from satellites can be affected by clouds (Kobayashi & Dye, 2005). The effects of clouds during ± 2 compositing periods (a total of five consecutive samples: ± 16 days for MODIS and ± 20 days for SPOT-VEGETATION) around SOS and EOS were evaluated based on the cloud flag information. For MODIS, when the two cloud-

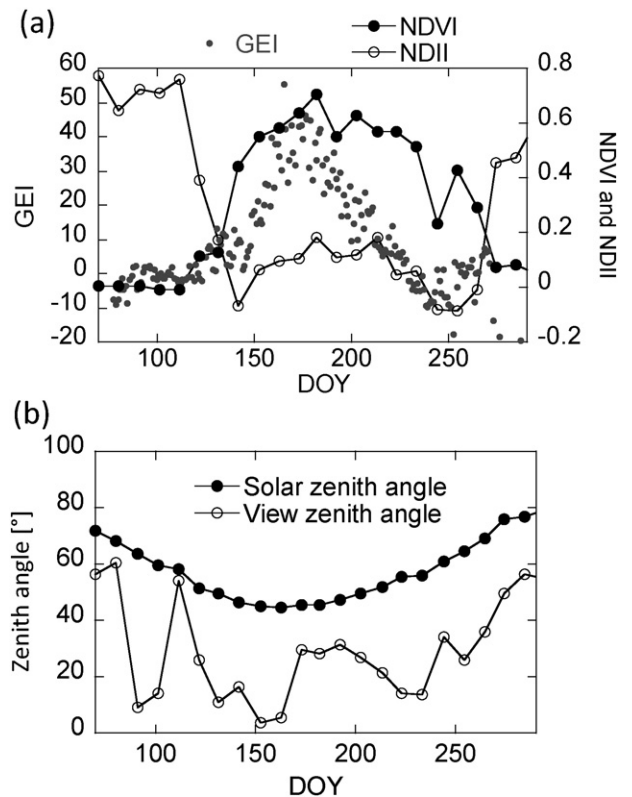


Fig. 3. (a) Comparison among GEI, NDVI, and NDII seasonality at F-1, 2011. VIs from SPOT-VEGETATION are plotted. (b) Solar and view zenith angles.

Table 2

Seasonal periods, solar zenith angles (SZA), optical parameters of understory vegetation, and overstory LAI seasonality employed in the radiative transfer simulation.

	DOY	SZA	Understory reflectance		Leaf area index			
			Red	NIR	Canopy Cover = 15%		Canopy Cover = 45%	
					20% change	50% change	20% change	50% change
Spring-1 w/snow	140 (May 20th)	47.57°	0.561	0.466	0.58	0.37	1.9	1.2
Spring-2	140 (May 20th)	47.57°	0.0737	0.294	0.58	0.37	1.9	1.2
Summer-1	182 (Jul. 1st)	44.31°	0.0527	0.330	0.73	0.73	2.4	2.4
Summer-2	213 (Aug. 1st)	49.14°	0.0527	0.330	0.73	0.73	2.4	2.4
Autumn-1	244 (Sep. 1st)	58.62°	0.0737	0.294	0.58	0.37	1.9	1.2
Autumn-2	274 (Oct. 1st)	69.93°	0.0737	0.294	0.58	0.37	1.9	1.2
Autumn-3 w/snow	274 (Oct. 1st)	69.93°	0.561	0.466	0.58	0.37	1.9	1.2

related bits in the State Flag data were both zero, we considered the data to have no cloud contamination; otherwise, the observation was considered to be partially or fully affected by clouds. Similarly, for SPOT-VEGETATION data, when the two cloud-related bits in the Status Map (SM) data were both zero, we considered the data to be cloud-free; otherwise, the observation was considered to be partially or fully affected by clouds. Cloud fractions (%) for each location were quantified as the proportion of the number of cloudy samplings in ± 2 compositing periods during SOS and EOS events.

2.3.2. Determination of the snow events

The last and first dates of lingering snowpack were evaluated by the time-lapse camera images. We followed the criteria provided by Sugiura et al. (2013), which is: (1) when the length of lingering snowpack cover exceeds 30 consecutive days, the period from the first day to the last day is the period of lingering snowpack and (2) “the existence of snow cover” is the condition, in which more than half of the surface is covered by snow. Based on their criteria, we determined the last (snowmelt) and first (snowfall) dates of lingering snowpack from time-series images.

2.4. Radiative transfer simulation

A three-dimensional Monte Carlo ray-tracing radiative transfer simulation was performed to examine the cause of seasonality in satellite spectral reflectance over sparse black spruce forest sites. In this study,

a spatially explicit three-dimensional model, the Forest Light Environmental Simulator (FLiES), was employed to simulate bidirectional reflectance seasonality in red and NIR (Kobayashi & Iwabuchi, 2008; Kobayashi et al., 2012). The performance and reliability of FLiES for simulating light transmittance through a canopy and bidirectional reflectance factors have been investigated in the previous works (Widowski et al., 2011, 2013). Required inputs for the model include simulated forest landscape data including individual tree position and size. The shape of the tree crown was abstracted as a spheroid and the crown objects were divided into two domains: the outer domains were filled with leaves and inner domains were filled with woody materials.

Forest landscape data were constructed based on the field census measurements at the F-6 site (PFA), which located ~32 km from Fairbanks, interior Alaska. Individual tree positions, canopy heights, and crown widths were based on the data of Kobayashi, Suzuki, Nagai, Nakai, and Kim (2014). The tree density, canopy cover, and maximum overstory leaf area index (LAI) were 3967 trees ha⁻¹, 15% and 0.73, respectively. We also constructed a denser forest landscape simulation based on the abovementioned data to understand how the characteristics of sparse tree stands in a black spruce affect the determination of SOS and EOS. In this landscape data, we maintained an identical tree density as the original data and doubled the size of crown heights and crown widths. The canopy cover and maximum overstory LAI of this denser landscape were 45% and 2.4, respectively. There are minor, but

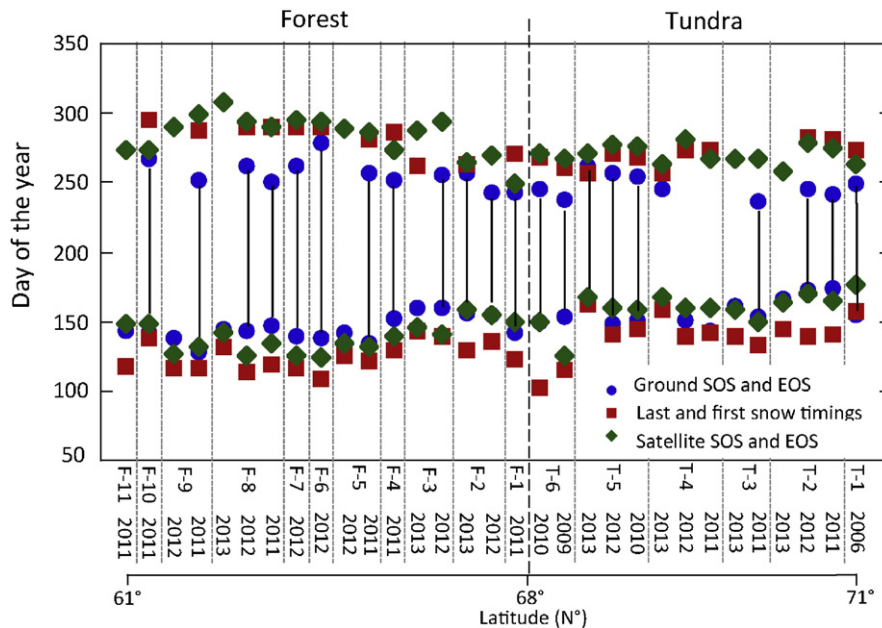


Fig. 4. Summary of the satellite-derived SOS and EOS (green diamond), the last (spring) and first (autumn) snow timings (red rectangle), and the ground-based SOS and EOS (blue circle). The black bars indicate the growing season determined by the ground-based time-lapse cameras. The satellite-derived SOSs and EOSs were the average of all methods derived from two satellite datasets (SPOT-VEGETATION and Terra-MODIS).

non-negligible seasonal changes of overstory LAI even in boreal evergreen forests (Chen, 1996). To consider this seasonal changes and the potential contamination of minor deciduous trees in evergreen spruce forests, we performed the simulation for three different seasonal overstory LAI conditions: (1) constant overstory LAI throughout the season, (2) overstory LAI changes seasonally by 20%, and (3) overstory LAI changes seasonally by 50% (Table 2).

Seasonal changes in understory optical data are summarized in Table 2 based on measurements reported in Kobayashi et al. (2014). Other optical variables—such as needle reflectance and transmittance, and woody reflectance—were 0.0741, 0.0232, and 0.0509 in red and 0.466, 0.387, and 0.0906 in NIR, respectively. These variables were constant throughout the season. We simulated five days from spring to autumn. In spring (DOY 140) and autumn (DOY 274) (Table 2), two understory conditions were simulated: with and without snow. The reflectance of snow value used was measured by Suzuki et al. (2011). The solar zenith angles of the simulated conditions were near the satellite overpass time (LST 10:30 am).

3. Results

The satellite-based SOS and EOS, the ground-based SOS and EOS, and the last (spring) and first (autumn) lingering snowpack dates estimated for each site and year are summarized in Fig. 4. The growing season lengths (the black bar between SOS and EOS) from the ground-based time-lapse images were quantified for 21 out of 31 cases (site × year) (see Supplemental Fig. 1). For the other 10 cases, due to bad quality or missing images, the image data from spring to autumn were not fully available. For those sites, we only estimated one of two phenology timings (SOS or EOS) depending on the data availability. The date of ground-based SOS and EOS were determined by the analysis shown in the following section (Section 3.1). The satellite-based SOS and EOS in Fig. 4 are the ensemble of all methods estimated from two satellite datasets (SPOT-VEGETATION and Terra-MODIS). Overall, correlation coefficients (*R*) of ground-based and satellite-based events were 0.64 for SOS and 0.49 for EOS, respectively. The error estimates for the methods used are described in Section 3.2 and Fig. 5.

3.1. SOS and EOS derived from time-lapse photography

In the spring period, *D*₁ was 10.3 days earlier than *D*_{SOS,V} and *D*₂ was 46.0 days later than *D*_{SOS,V} on average. The *D*_{SOS,V} was thus consequently represented by *D*_{1,75%} + *D*_{2,25%} (the weighted average of *D*₁ [75% weight] and *D*₂ [25% weight]). The mean bias of *D*_{1,75%} + *D*_{2,25%} was 1.2 days (Table 3). In the autumn period, both *D*₃ and *D*₄ were earlier

Table 3

Comparison of visually determined SOS and EOS (*D*_{SOS,V} and *D*_{EOS,V}) with GEI-based onset and offset timings. We examined this visual interpretation only for the sites (F-1, F-4, F-5, F-7, F-9, F-10, and F-11 in Table 1), at which cameras were installed near the target plants.

Site	Year	<i>D</i> _{SOS,V}	<i>D</i> ₁	<i>D</i> ₂	<i>D</i> ₁ 75% + <i>D</i> ₂ 25%	<i>D</i> _{EOS,V}	<i>D</i> ₃	<i>D</i> ₄
F-1	2011	149	131	173	141.5	234	169	238
F-4	2011	150	144	176	152.0	234	207	247
F-5	2011	136	118	181	133.8	254	206	252
	2012	132	128	185	142.3	–	–	–
F-7	2012	139	131	166	137.8	–	–	–
F-9	2011	122	109	186	128.3	281	195	247
	2012	145	120	190	137.5	–	–	–
F-10	2011	146	136	158	141.5	269	222	262
F-11	2011	124	135	166	142.8	–	–	–
	2012	147	135	166	142.8	–	–	–
Average	–	139.0	128.7	174.7	140.2	254.4	199.8	249.2
Bias	–	–	–10.3	46.0	1.2	–	–54.6	–5.2
RMSE	–	–	13.2	37.2	7.8	–	58.1	16.7

*D*₁: green-up, *D*₂: maturity, *D*₃: senescence, *D*₄: dormancy.

than *D*_{EOS,V} (54.6 days for *D*₃ and 5.2 days for *D*₄). The ground-based EOS was represented by *D*₄ – 5.2 days.

3.2. Comparison of various satellite-based SOSs and EOSs with ground-based SOS (*D*_{SOS,V}) and EOS (*D*_{EOS,V})

The biases of the estimated SOS and EOS were diverse among the methods (Fig. 5). Among three satellite-based methods for determining SOS and EOS, no particular method was most consistent with the ground-based measurement. In spring, the satellite-based SOS was between 2.9 and 12.7 days earlier (positive biases) than the ground-based SOS in boreal forest sites, excepting the NDII method. In tundra sites, direction of the biases varied by the methods employed. Three methods (NDVI_S, NDII_S, NDII_M) calculated SOS later than the ground-based SOS (bias = –6.9 days [SOS (NDVI_S)], –16.4 days [SOS (NDII_S)], and –13.3 days [SOS (NDII_M)] and three methods (NDVI_M, Logistic_S, Logistic_M) calculated an earlier SOS than the ground-based SOS (bias = 10.2 days [SOS (NDVI_M)], 3.4 days [SOS (Logistic_S)], and 10.0 days [SOS (Logistic_M)]).

The NDII method showed the smallest biases (0.26 days for SOS (NDII_S) and –0.58 days for SOS (NDII_M)) and RMSEs (9.4 and 10.0 days) for forest sites. However, in tundra sites, both the biases and RMSE for the NDII method were largest among the methods (–16.4 days for SOS (NDII_S) and –13.3 days for SOS (NDII_M)) and RMSEs (30.3 and 20.4 days). The surface in most tundra sites is inundated just after snowmelt and NDII is sensitive to not only the amount of

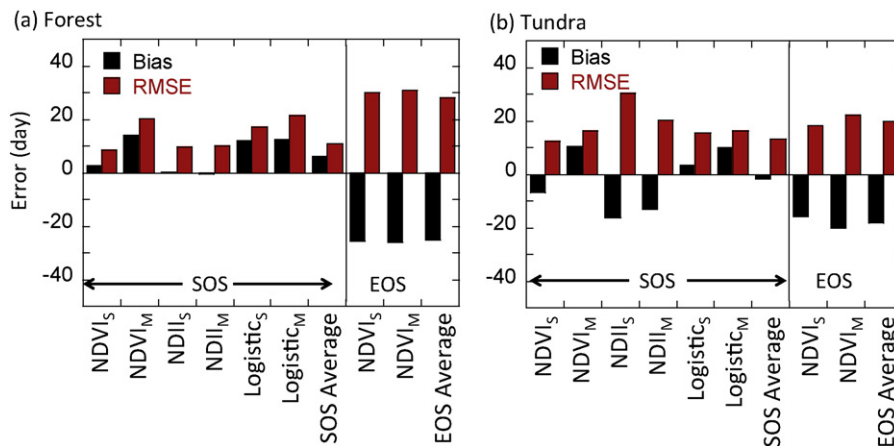


Fig. 5. The mean bias and root mean square errors of the satellite-derived SOS and EOS results. The subscripts “S” and “M” stand for SPOT-VEGETATION and Terra-MODIS. The positive bias indicates that the satellite-derived SOS and EOS timings are earlier than ground-based timings. (a) Forest sites, (b) tundra sites.

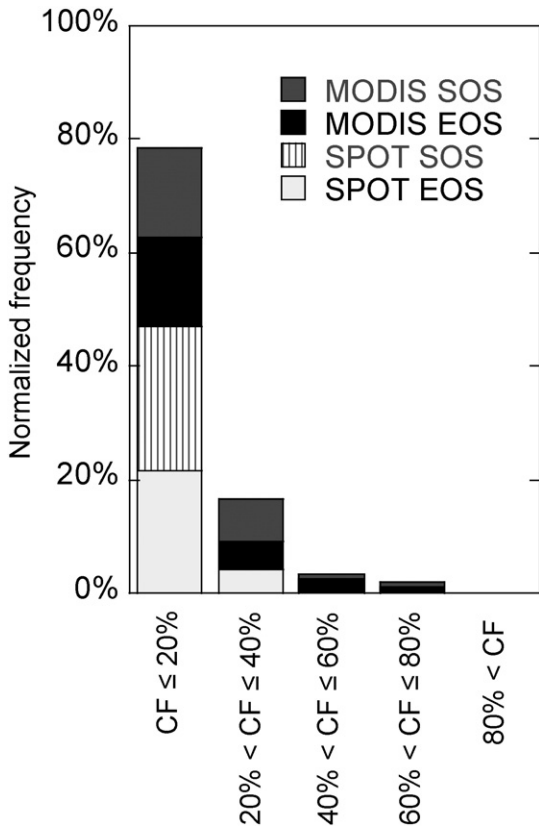


Fig. 6. Normalized frequency of cloud fractions (CF, %). Cloud fractions were quantified as the proportion of the number of cloudy samplings in ± 2 compositing periods during the SOS and EOS events.

vegetation but also the surface wetness. Therefore, the NDII did not drop rapidly after snowmelt, but rather gradually decreased as a combined effect of wetness and green vegetation development from spring to

summer. Consequently, the date of the minimum NDII, which is considered as SOS, was delayed until around the early summer.

For autumn EOS, the large differences between satellite-based and ground-based EOSs were found for both boreal forest (mean bias -25.7 days and RMSE 30.2 days for SPOT-VEGETATION and mean bias -26.0 days and RMSE 30.7 days for MODIS) and tundra sites (mean bias -16.0 days and RMSE 18.4 days for SPOT-VEGETATION and mean bias -20.3 days and RMSE 22.3 days for MODIS). The differences for boreal forest sites were 5.7 days (MODIS) to 9.7 days (SPOT-VEGETATION) days greater than those of tundra. The possible causes of these EOS differences are analyzed in Section 3.4.

Persistent cloud cover potentially introduces errors to the estimation of the increase in SOS and EOS. In our study sites and periods, 78.5% of SOSs and EOSs were estimated under low cloud atmospheric conditions ($CF < 20\%$) (Fig. 6). As the SPOT-VEGETATION S10 has longer compositing periods, the cloud fraction of SPOT-VEGETATION was less than that of MODIS. For both SPOT-VEGETATION and MODIS, the cloud fractions during EOS were larger than during SOS. The increase in cloud fraction is prone to cause later SOS or earlier EOS estimates, which is the opposite of the bias direction in our results (Fig. 5). Thus, our result implies that, while the effects of cloud were marginal at our study sites, the effects of the cloud cover potentially underestimated the bias in SOS and EOS evaluated in Fig. 5.

3.3. Latitudinal gradient of snow and phenology timings

The timing of snow cover and phenological events in 2011 and 2012 showed consistent latitudinal gradients across the forest-tundra ecotone in the study area (Fig. 7). The relative timing of snow (snowmelt in spring and snowfall in autumn) versus ground-based and satellite based phenology differed between spring and autumn periods. In spring, the snowmelt preceded satellite-based and ground-based SOS by 16 to 19 days. In autumn, the ground-based EOS preceded satellite-based EOS by 19 to 26 days and the satellite-based EOS almost coincided with the snow events. For both years, the latitudinal gradient of phenological events (slopes shown in Fig. 7) were steeper in spring than those in autumn, except for the case of spring snowmelt in 2011. The

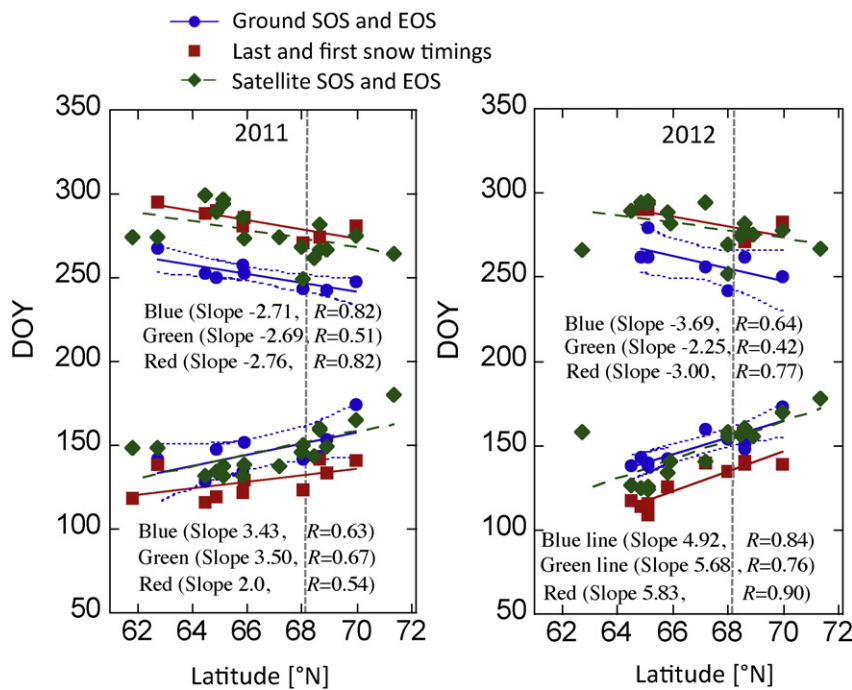


Fig. 7. Latitudinal gradients of satellite-derived SOS and EOS, last and first snow timings, and phenological timings (SOS and EOS) derived from time-lapse cameras in 2011 and 2012. The satellite-derived SOS and EOS are the averages of three method and two satellite datasets. Gray dotted lines show the forest-tundra ecotone. For ground-based SOS and EOS, the 95% confidence intervals are also plotted.

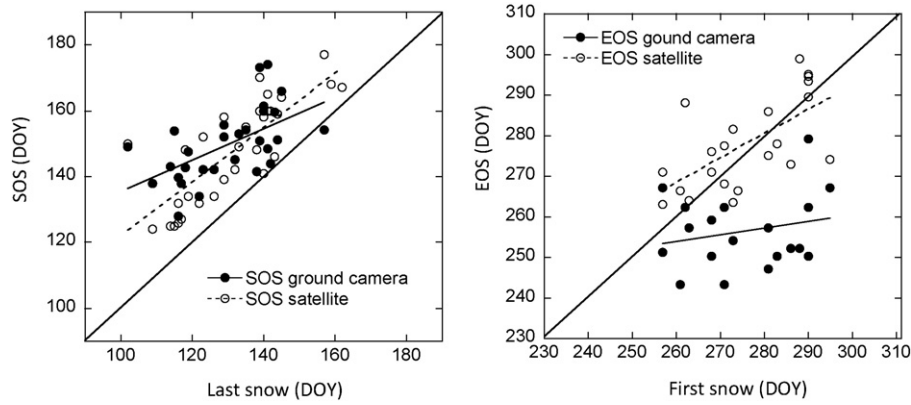


Fig. 8. The relationship between the snow timings (the last and the first snow) and plant phenology metrics (SOS and EOS). The correlation coefficients for the SOS satellite and SOS ground camera are $R = 0.79$ ($p < 0.01$) and 0.58 ($p < 0.01$), respectively. The correlation coefficients for the EOS satellite and EOS ground camera are $R = 0.63$ ($p = 0.017$) and $R = 0.19$ ($p = 0.88$), respectively.

latitudinal gradients of the ground-based SOS and EOS were $3.4 \text{ days degree}^{-1}$ and $-2.7 \text{ days degree}^{-1}$ for 2011 and $4.9 \text{ days degree}^{-1}$ and $-3.7 \text{ days degree}^{-1}$ for 2012, respectively. The latitudinal gradients of air temperature in spring (May) and autumn (an average of August and September) were $-1.4 \text{ }^\circ\text{C degree}^{-1}$ and $-0.89 \text{ }^\circ\text{C degree}^{-1}$ in 2011 and $-1.3 \text{ }^\circ\text{C degree}^{-1}$ and $-0.81 \text{ }^\circ\text{C degree}^{-1}$ in 2012, respectively. Thus, the changes in SOS with regard to air temperature ($dSOS/dT_a$) were $-2.5 \text{ days }^\circ\text{C}^{-1}$ in 2011 and $-3.9 \text{ days }^\circ\text{C}^{-1}$ in 2012. The changes in EOS with regard to air temperature ($dEOS/dT_a$) were $3.0 \text{ days }^\circ\text{C}^{-1}$ and $4.6 \text{ days }^\circ\text{C}^{-1}$ in 2011 and in 2012, respectively.

The correlation between EOS and the timing of snow cover onset was weaker than that between SOS and the timing of snowmelt (Fig. 8). The correlation coefficients of satellite-based and ground-based SOSs against the latest continuous snow date were 0.79 ($p < 0.01$) and 0.58 ($p < 0.01$), respectively. On the other hand, the correlation coefficients of satellite-based and ground-based EOSs against

the earliest continuous snow date were 0.63 ($p = 0.017$) and 0.19 ($p = 0.88$), respectively.

3.4. Simulated seasonal variations in NDVI and phenology timing

The simulated NDVI displayed seasonal patterns that were typical of those observed in the satellite NDVI data (Fig. 9). Although NDVI depends on satellite view angles, those geometries (three view zenith and azimuthal angle cases in Fig. 9) did not result in substantial differences in NDVI (coefficient of variation $< 3.5\%$) except for the snow periods (up to 28%).

The understory reflectivity accounts for 86–99% in red and 65–83% in NIR (canopy cover = 15%) (Fig. 9d–f) and 48–97% in red and 25–66% in NIR (canopy cover = 45%) (view zenith angle and azimuth angle = 0°) (Fig. 9a–c). After the snowmelt, NDVI increased during the summer (summer-2) because of the decrease in understory red reflectance and increase in the NIR reflectance (Table 2). However, this

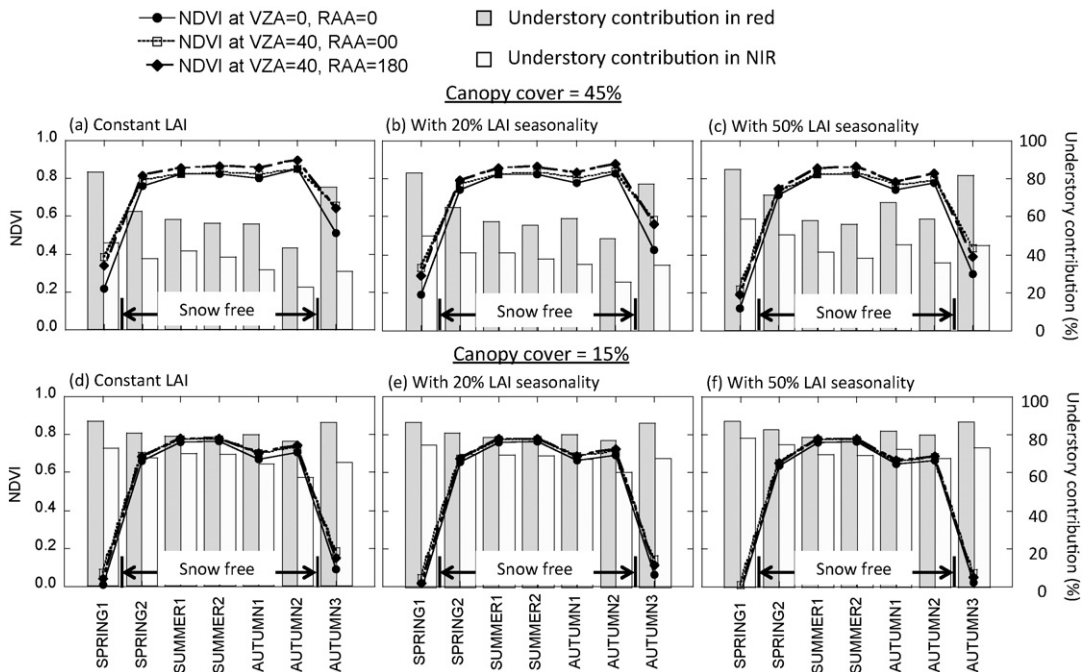


Fig. 9. The simulated seasonal patterns in NDVI (lines) for two different canopy (overstory) coverages and three different seasonal changes in overstory leaf area index (LAI). (a–c) Canopy cover = 45% and (d–f) canopy cover = 15%. (a) and (d) Constant overstory LAI throughout the season; (b) and (e) overstory LAI varies 20% seasonally; (c) and (f) overstory LAI varies 50% seasonally. The three lines in each figure show the different view zenith angles (VZAs) and satellite azimuth angles relative to the sun (RAA). The dark and light gray colored bars are the contribution of reflected radiance in the red and NIR spectral regions.

NDVI increase (spring-1 to summer-2) accounted for only 8.6–17% of total NDVI seasonal amplitude (Fig. 9a–f).

Seasonal variations in NDVI were caused by the contribution of understory observed from the satellite (Fig. 9). The results slightly depended on the zenith and azimuth angles, but the seasonal changes were similar among the satellite view angles. The reflectance contribution of the understory gradually decreased from spring-1 to autumn-2, indicating that satellites view more of the canopy overstory (greener needles) rather than brownish understory. Moreover, this seasonal change of overstory and understory contributions was larger in the red domain than that in the NIR domain. Consequently, the NDVI in late autumn was greatly influenced by the greener overstory needles. In addition, the NDVI in late autumn (autumn-2) increased again under both canopy cover of 15% and 45% conditions due to the very high solar zenith angle.

The seasonality in overstory LAI caused the changes in the NDVI seasonality. For example, the constant overstory LAI case (Fig. 9a) exhibits almost constant NDVI throughout the growing season (from spring-2 to autumn-1). In contrast, the overstory LAI with 50% seasonality exhibits the bell-shaped NDVI seasonal patterns (Fig. 9c). Changes of up to 50% in overstory LAI caused 6.0–9.0% differences in the NDVI for a canopy cover of 45% (Fig. 9a–c), and 3.3–4.9% differences for a canopy cover of 15% (Fig. 9d–f). As the LAI seasonality increased, the reflectance was more influenced by the understory in the spring and autumn rather than greener overstory, and the seasonal amplitude of NDVI ($NDVI_{max} - NDVI_{min}$) was enhanced from 0.55 to 0.66 (with snow season) and 0.078 to 0.106 (snow free period) for a canopy cover of 45% and 0.73 to 0.78 (with snow season) and 0.096 to 0.125 (snow free period).

4. Discussion

In spring phenology, satellite-based SOS metrics are known to be partially affected by the snowmelt in the Arctic and sub-Arctic regions (Dye & Tucker, 2003). Despite this issue, the satellite-based SOS may be related to leaf emergence in spring because leaf emergence happens immediately after the snowmelt. We estimated SOSs using multiple methods and data in Alaska to avoid the bias due to the method employed (White et al., 2009). Based on the comparison of six satellite-based SOSs (Fig. 5), we recommend using an ensemble average SOS because individual methods showed relatively high errors and their tendencies varied with the ecosystem type (forest or tundra). In fact, the ensemble SOS was the best performing of the methods employed (Fig. 5). NDVI_s showed a relatively good performance in our comparison (Fig. 5); however, a single method and satellite data potentially leads to erroneous results due to atmospheric influence (e.g. residual clouds). Indeed, our comparison revealed that the NDII based methods (NDII_s and NDII_M) had the largest biases (−13.3 to −16.4 days) while Delbart and Picard (2007) found that the bias between satellite-based SOS calibrated by NDII and the ground SOS measurements near the Toolik lake (close to the T-4 & T-5 sites) was less than our results (−3.25 days). This was potentially caused by the periods compared, the difference in the satellite data used, atmospheric conditions, and the differences of the ground phenology observation methods. The satellite-based SOS was slightly earlier than the ground-based SOS, but its latitudinal gradient was consistent with the leaf appearance of the forest understory and tundra vegetation (Fig. 7). Thus the satellite-based SOS can be useful as a measure of spring tundra and forest understory leaf emergences.

The consistency between the ground-based and satellite-based EOSs was weaker than the relationship of ground-based and satellite-based SOS for boreal forest and tundra sites because of large biases between those two EOSs (19 to 26 days, Fig. 7). The satellite-based EOS was more relevant to the first date of lingering snowpack. On the other hand, the ground-based EOS was independent of snow events (Fig. 8). At tundra sites, the EOS biases were smaller than those of boreal forest sites. This is because, unlike the black spruce forests, the deciduous

plants are directly exposed on the canopy surface. The leaf color change can be directly viewed from satellites. However, due to the abrupt decrease in NDVI caused by snowfall, the NDVI threshold (defined as 50% of the NDVI seasonal amplitude) did not correspond with EOS events. In addition to the lingering snowpack, there may be other issues on the uncertainty of the EOS estimation. Nagai et al. (2014) found that the autumn phenology in a cool-temperate deciduous broad-leaved forest occurred continuously because of different phenological timings among species and their spatial heterogeneities. This causes the additional uncertainty in determining the EOS.

Beck et al. (2007) proposed a different threshold for spring and autumn phenology events. Using their approach the EOS is determined by a higher threshold value. If the variation in reflectance in tundra plants is similar to the understory reflectance in boreal forests (Table 2), the EOS in tundra sites may be estimated to be 84% of the NDVI seasonal amplitude. In boreal forest sites, however, it may not be straightforward to calibrate the biases between satellite-based and ground-based EOS in boreal forests by simply adjusting the threshold. The plant canopy radiative transfer simulation suggests that the appropriate NDVI threshold can vary with the canopy cover, overstory LAI seasonality, and solar zenith angles (Fig. 9). Assuming that the crown cover of 15% in Fig. 9 is more common in Alaska, the EOS in forest sites may be estimated to be 86% of the NDVI seasonal amplitude when overstory LAI is assumed to be constant throughout the growing season. For the determination of the appropriate threshold, a reliable forest cover map is required. Also, evergreen boreal forests show a little LAI seasonality (Chen, 1996). This weak seasonality does not significantly affect the NDVI threshold in sparse forest; however, as the canopy cover increases or minor deciduous trees contaminate the spectral signals, the NDVI threshold is likely to be affected by those overstory seasonal changes.

The time-lapse cameras provide precise in-situ phenology measurements that can be used for the validation of satellite phenology estimates. When applying this technique to boreal forest understory, there are several issues to be carefully considered due to the limitations of image quality and the region of interest in camera images. The species composition within the camera images influences the timing of phenological events. At our study sites, the regions of interest of the understory vegetation within the camera images were defined to be as large as possible to avoid an irregular phenological pattern of particular plants and to obtain the average signature of different plants. Although most evergreen forest understory is covered with herbaceous plants, deciduous dwarfs, moss, and lichen as described in Section 2.1, the species composition in camera images was not identical. This could cause uncertainty in obtaining the average understory phenology in each forest site. Likewise, we focused on the phenology of herbaceous plants and dwarf trees. While Moss and lichen also show seasonally, it was not taken into consideration in this study. However, even if moss and lichen are present, because they grow under the herbaceous plants and dwarf trees, their phenological changes may have less impact on the satellite signal. The effect of moss and lichen should be investigated further through much finer-resolution images, with information regarding the spatial fraction of each element.

The timings of SOS and EOS along 61°N to 71°N derived from satellite and time-lapse camera images revealed the latitudinal gradients from both measurements were almost consistent. Zhu et al. (2012) estimated the latitudinal gradients of SOS and EOS across the North American continent from 35°N to 70°N. The exact comparison may not be appropriate because of the difference in satellite data used (NOAA-AVHRR GIMMS), study periods (1982 to 2006) and area (North America). However, it is interesting to compare the consistency of both results. The rate of change calculated by Zhu et al. (2012) was 2.6 days degree^{−1} for SOS and −2.8 days degree^{−1} for EOS for 35°N to 70°N. When evaluated from 60°N to 70°N (from Fig. 2 in Zhu et al. (2012)), both SOS and EOS were approximately 2.5 days degree^{−1} and −2.5 days degree^{−1}. This study showed 3.5 to 5.7 days degree^{−1}

for SOSs and -2.3 to -2.7 days degree $^{-1}$ for EOSs, respectively. Zhu et al. (2012) reported latitudinal symmetry for SOS and EOS, but we found a higher latitudinal gradient in SOS than in EOS, indicating that the SOS was less sensitive to changes in air temperature ($dSOS/dT_a$ of -2.5 to -3.9 days $^{\circ}\text{C}^{-1}$) than EOS ($dEOS/dT_a$ of 3.0 to 4.6 days $^{\circ}\text{C}^{-1}$).

The average air temperature in the Arctic region rose up to 1.36 $^{\circ}\text{C}$ in the first decade of the 21st century (Bekryaev et al., 2010; Hinzman et al., 2013). If the timings of SOS and EOS were only regulated by air temperature, it would be expected that the temperature increase would have an impact on the timing of phenological events in the Arctic. Assuming $dSOS/dT_a$ and $dEOS/dT_a$ evaluated from the latitudinal gradient of phenology and air temperature (Fig. 7) are used for decadal scale phenology change, in the first decade of the 21st century SOS may be 4.4 days earlier and EOS 5.2 days later following a 1.36 $^{\circ}\text{C}$ warming across the state of Alaska. This assumption derived from the temperature dependency of phenology should be validated by a more detailed analysis based on long-term ground-based observations.

5. Conclusion

The satellite-retrieved SOS and EOS have been extensively used for large-scale phenological studies. Despite their numerous spatial and trend analyses in SOS and EOS, there is still little information on how the latitudinal gradient of satellite-based SOS and EOS are related to changes in seasonal surface condition (e.g., snow), plant phenology, and satellite observation conditions in the Arctic and sub-Arctic regions. Using time-lapse camera images collected at 17 sites across Alaska, we quantified the phenological events along the latitudinal range from 61°N to 71°N . In SOS events, we found that the satellite-based SOS can be a measure of spring understory and tundra plants green-up when the SOS values estimated by multiple methods are averaged. A large difference was revealed between ground-based and satellite-based EOS. The satellite-based EOS was much more relevant to snowfall events than the senescence of understory and tundra plants in Alaska. While there are several limitations in using satellite- and ground-based phenology estimates, quantification of latitudinal gradient of phenology can be useful information in understanding the influence of warming to plant phenological timings. As understory plants in black spruce forests have a significant impact on the carbon exchanges, the reliable information of understory plants phenology is important. Our study demonstrates the possible impact of phenology in spruce forest understory and tundra ecosystems in response to climate change in the warming Arctic and sub-Arctic regions.

Supplementary data to this article can be found online at <http://dx.doi.org/10.1016/j.rse.2016.02.020>.

Acknowledgements

This research was supported by the Environment Research and Technology Development Fund (RFa-1201) of the Ministry of the Environment, the JAMSTEC-IARC Collaboration Study (JICS), and the Japan Society for the Promotion of Science (JSPS) KAKENHI Grant (Numbers 25281014 and 20281003). Time-lapse images from Toolik Lake were taken with support from a National Science Foundation grant #1048361. We thank Jeb Timm for his support installing and troubleshooting the Toolik Field Station time-lapse cameras and Kyoko Ikeda for helping the data processing of the phenology camera images. The site maintenance at CT, UT, TZ, and BC was partly supported by a National Research Foundation of Korea Grant from the Korean Government (MSIP) (NRF-C1ABA001-2011-0021063; PI: Bang-Yong Lee) (KOPRI-PN15081) (CAPEC Project)). We also thank three anonymous reviewers and Dr. Nicolas Delbart for their constructive comments.

References

- Barichivich, J., Briffa, K. R., Myneni, R. B., Osborn, T. J., Melvin, T. M., Ciais, P., ... Tucker, C. (2013). Large-scale variations in the vegetation growing season and annual cycle of atmospheric CO_2 at high northern latitudes from 1950 to 2011. *Global Change Biology*, 19, 3167–3183.
- Beck, P. S. A., Jonsson, P., Hogda, K. A., Karlsen, S. R., Eklundh, L., & Skidmore, A. K. (2007). A ground-validated NDVI dataset for monitoring vegetation dynamics and mapping phenology in Fennoscandia and the Kola peninsula. *International Journal of Remote Sensing*, 28, 4311–4330.
- Bekryaev, R. V., Polyakov, I. V., & Alexeev, V. A. (2010). Role of polar amplification in long-term surface air temperature variations and modern Arctic warming. *Journal of Climate*, 23, 3888–3906.
- Buermann, W., Parida, B., Jung, M., MacDonald, G. M., Tucker, C. J., & Reichstein, M. (2014). Recent shift in Eurasian boreal forest greening response may be associated with warmer and drier summers. *Geophysical Research Letters*, 41, 1995–2002.
- Chen, J. M. (1996). Optically-based methods for measuring seasonal variation of leaf area index in boreal conifer stands. *Agricultural and Forest Meteorology*, 80, 135–163.
- Delbart, N., & Picard, G. (2007). Modeling the date of leaf appearance in low-arctic tundra. *Global Change Biology*, 13, 2551–2562.
- Delbart, N., Kergoat, L., Le Toan, T., Lhermitte, J., & Picard, G. (2005). Determination of phenological dates in boreal regions using normalized difference water index. *Remote Sensing of Environment*, 97, 26–38.
- Delbart, N., Picard, G., Le Toans, T., Kergoat, L., Quegan, S., Woodward, I., ... Fedotova, V. (2008). Spring phenology in boreal Eurasia over a nearly century time scale. *Global Change Biology*, 14, 603–614.
- Delpierre, N., Dufrene, E., Soudani, K., Ulrich, E., Cecchini, S., Boe, J., & Francois, C. (2009). Modelling interannual and spatial variability of leaf senescence for three deciduous tree species in France. *Agricultural and Forest Meteorology*, 149, 938–948.
- Dye, D. G., & Tucker, C. J. (2003). Seasonality and trends of snow-cover, vegetation index, and temperature in northern Eurasia. *Geophysical Research Letters*, 30.
- Environmental Data Center Team (2014). Snow-cover monitoring program at Toolik, Alaska. *Toolik Field Station, Institute of Arctic Biology*. Fairbanks: University of Alaska Fairbanks AK 99775. http://toolik.alaska.edu/edc/image_library.php.
- Euskirchen, E. S., Bret-Harte, M. S., Scott, G. J., Edgar, C., & Shaver, G. R. (2012). Seasonal patterns of carbon dioxide and water fluxes in three representative tundra ecosystems in northern Alaska. *Ecosphere*, 3.
- Forkel, M., Carvalhais, N., Rödenbeck, C., Keeling, R., Heimann, M., Thonicke, K., ... Reichstein, M. (2016). Enhanced seasonal CO_2 exchange caused by amplified plant productivity in northern ecosystems. *Science*, aac4971.
- Garonna, I., De Jong, R., De Wit, A. J. W., Mucher, C. A., Schmid, B., & Schaepman, M. E. (2014). Strong contribution of autumn phenology to changes in satellite-derived growing season length estimates across Europe (1982–2011). *Global Change Biology*, 20, 3457–3470.
- Goetz, S. J., Bunn, A. G., Fiske, G. J., & Houghton, R. A. (2005). Satellite-observed photosynthetic trends across boreal North America associated with climate and fire disturbance. *Proceedings of the National Academy of Sciences of the United States of America*, 102, 13521–13525.
- Hardisky, M. A., Klemas, V., & Smart, R. M. (1983). The influence of soil-salinity, growth form, and leaf moisture on the spectral radiance of *Spartina-Alterniflora* canopies. *Photogrammetric Engineering and Remote Sensing*, 49, 77–83.
- Harris, I., Jones, P. D., Osborn, T. J., & Lister, D. H. (2014). Updated high-resolution grids of monthly climatic observations – the CRU TS3.10 dataset. *International Journal of Climatology*, 34, 623–642.
- Hinzman, L. D., Deal, C. J., McGuire, A. D., Mernild, S. H., Polyakov, I. V., & Walsh, J. E. (2013). Trajectory of the Arctic as an integrated system. *Ecological Applications*, 23, 1837–1868.
- Hogda, K. A., Tommervik, H., & Karlsen, S. R. (2013). Trends in the start of the growing season in Fennoscandia 1982–2011. *Remote Sensing*, 5, 4304–4318.
- Ikawa, H., Nakai, T., Busey, R. C., Kim, Y., Kobayashi, H., Nagai, S., ... Suzuki, R. (2015). Understory CO_2 , sensible heat, and latent heat fluxes in a black spruce forest in interior Alaska. *Agricultural and Forest Meteorology*, 214, 80–90.
- IPCC (2013). The physical science basis. *Contribution of Working Group I to the Fifth Assessment Report of the Intergovernmental Panel on Climate Change*. Cambridge: United Kingdom and New York, NY, USA.
- Iwata, H., Ueyama, M., Harazono, Y., Tsuyuzaki, S., Kondo, M., & Uchida, M. (2011). Quick recovery of carbon dioxide exchanges in a burned black spruce forest in interior Alaska. *Sola*, 7, 105–108.
- Iwata, H., Ueyama, M., Iwama, C., & Harazono, Y. (2013). A variation in the fraction of absorbed photosynthetically active radiation and a comparison with MODIS data in burned black spruce forests of interior Alaska. *Polar Science*, 7, 113–124.
- Jeong, S. -J., & Medvigy, D. (2014). Macroscale prediction of autumn leaf coloration throughout the continental United States. *Global Ecology and Biogeography*, 23, 1245–1254.
- Jeong, S. -J., Ho, C. -H., Gim, H. -J., & Brown, M. E. (2011). Phenology shifts at start vs. end of growing season in temperate vegetation over the Northern Hemisphere for the period 1982–2008. *Global Change Biology*, 17, 2385–2399.
- Jonsson, A. M., Eklundh, L., Hellstrom, M., Barring, L., & Jonsson, P. (2010). Annual changes in MODIS vegetation indices of Swedish coniferous forests in relation to snow dynamics and tree phenology. *Remote Sensing of Environment*, 114, 2719–2730.
- Keenan, T. F., Gray, J., Friedl, M. A., Toomey, M., Bohrer, G., Hollinger, D. Y., ... Richardson, A. D. (2014). Net carbon uptake has increased through warming-induced changes in temperate forest phenology. *Nature Climate Change*.
- Kim, Y. (2014). Effect of ablation rings and soil temperature on 3-year spring CO_2 efflux along the Dalton Highway, Alaska. *Biogeosciences*, 11, 6539–6552.

- Kim, Y., Kodama, Y., Shim, C., & Kushida, K. (2014). Carbon exchange rates in *Polytrichum juniperinum* moss of burned black spruce forest in interior Alaska. *Polar Science*, 8, 146–155.
- Kobayashi, H., & Dye, D. G. (2005). Atmospheric conditions for monitoring the long-term vegetation dynamics in the Amazon using normalized difference vegetation index. *Remote Sensing of Environment*, 97, 519–525.
- Kobayashi, H., & Iwabuchi, H. (2008). A coupled 1-D atmosphere and 3-D canopy radiative transfer model for canopy reflectance, light environment, and photosynthesis simulation in a heterogeneous landscape. *Remote Sensing of Environment*, 112, 173–185.
- Kobayashi, H., Baldocchi, D. D., Ryu, Y., Chen, Q., Ma, S., Osuna, J. L., & Ustin, S. L. (2012). Modeling energy and carbon fluxes in a heterogeneous oak woodland: A three-dimensional approach. *Agricultural and Forest Meteorology*, 152, 83–100.
- Kobayashi, H., Delbart, N., Suzuki, R., & Kushida, K. (2010). A satellite-based method for monitoring seasonality in the overstory leaf area index of Siberian larch forest. *Journal of Geophysical Research-Biogeosciences*, 115.
- Kobayashi, H., Suzuki, R., & Kobayashi, S. (2007). Reflectance seasonality and its relation to the canopy leaf area index in an eastern Siberian larch forest: Multi-satellite data and radiative transfer analyses. *Remote Sensing of Environment*, 106, 238–252.
- Kobayashi, H., Suzuki, R., Nagai, S., Nakai, T., & Kim, Y. (2014). Spatial scale and landscape heterogeneity effects on FAPAR in an open-canopy black spruce forest in interior Alaska. *IEEE Geoscience and Remote Sensing Letters*, 11, 564–568.
- Kwon, H. J., Oechel, W. C., Zulueta, R. C., & Hastings, S. J. (2006). Effects of climate variability on carbon sequestration among adjacent wet sedge tundra and moist tussock tundra ecosystems. *Journal of Geophysical Research-Biogeosciences*, 111, 18.
- Myneni, R. B., Keeling, C. D., Tucker, C. J., Asrar, G., & Nemani, R. R. (1997). Increased plant growth in the northern high latitudes from 1981 to 1991. *Nature*, 386, 698–702.
- Nagai, S., Inoue, T., Ohtsuka, T., Kobayashi, H., Kurumado, K., Muraoka, H., & Nasahara, K. N. (2014). Relationship between spatio-temporal characteristics of leaf-fall phenology and seasonal variations in near surface- and satellite-observed vegetation indices in a cool-temperate deciduous broad-leaved forest in Japan. *International Journal of Remote Sensing*, 35, 3520–3536.
- Nagai, S., Nakai, T., Saitoh, T. M., Busey, R. C., Kobayashi, H., Suzuki, R., ... Kim, Y. (2013a). Seasonal changes in camera-based indices from an open canopy black spruce forest in Alaska, and comparison with indices from a closed canopy evergreen coniferous forest in Japan. *Polar Science*, 7, 125–135.
- Nagai, S., Saitoh, T. M., Kobayashi, H., Ishihara, M., Suzuki, R., Motohka, T., ... Muraoka, H. (2012). In situ examination of the relationship between various vegetation indices and canopy phenology in an evergreen coniferous forest, Japan. *International Journal of Remote Sensing*, 33, 6202–6214.
- Nagai, S., Saitoh, T. M., Kurumado, K., Tamagawa, I., Kobayashi, H., Inoue, T., ... Nasahara, K. N. (2013b). Detection of bio-meteorological year-to-year variation by using digital canopy surface images of a deciduous broad-leaved forest. *Sola*, 9, 106–110.
- Nakai, T., Kim, Y., Busey, R. C., Suzuki, R., Nagai, S., Kobayashi, H., ... Ito, A. (2013). Characteristics of evapotranspiration from a permafrost black spruce forest in interior Alaska. *Polar Science*, 7, 136–148.
- Oechel, W. C., Laskowski, C. A., Burba, G., Gioli, B., & Kalhori, A. A. M. (2014). Annual patterns and budget of CO₂ flux in an Arctic tussock tundra ecosystem. *Journal of Geophysical Research-Biogeosciences*, 119, 323–339.
- Piao, S., Ciais, P., Friedlingstein, P., Peylin, P., Reichstein, M., Luysaert, S., ... Vesala, T. (2008). Net carbon dioxide losses of northern ecosystems in response to autumn warming. *Nature*, 451, 49–53.
- Piao, S., Wang, X., Ciais, P., Zhu, B., Wang, T., & Liu, J. (2011). Changes in satellite-derived vegetation growth trend in temperate and boreal Eurasia from 1982 to 2006. *Global Change Biology*, 17, 3228–3239.
- Pisek, J., & Chen, J. M. (2009). Mapping forest background reflectivity over North America with Multi-angle Imaging SpectroRadiometer (MISR) data. *Remote Sensing of Environment*, 113, 2412–2423.
- Rahman, H., & Dedieu, G. (1994). SMAC: A simplified method for the atmospheric correction of satellite measurements in the solar spectrum. *Remote Sensing*, 15, 123–143.
- Rautiainen, M., & Heiskanen, J. (2013). Seasonal contribution of understory vegetation to the reflectance of a boreal landscape at different spatial Scales. *IEEE Geoscience and Remote Sensing Letters*, 10, 923–927.
- Richardson, A. D., Carbone, M. S., Keenan, T. F., Czimczik, C. I., Hollinger, D. Y., Murakami, P., ... Xu, X. M. (2013b). Seasonal dynamics and age of stemwood nonstructural carbohydrates in temperate forest trees. *New Phytologist*, 197, 850–861.
- Richardson, A. D., Jenkins, J. P., Braswell, B. H., Hollinger, D. Y., Ollinger, S. V., & Smith, M. L. (2007). Use of digital webcam images to track spring green-up in a deciduous broadleaf forest. *Oecologia*, 152, 323–334.
- Richardson, A. D., Keenan, T. F., Migliavacca, M., Ryu, Y., Sonnentag, O., & Toomey, M. (2013a). Climate change, phenology, and phenological control of vegetation feedbacks to the climate system. *Agricultural and Forest Meteorology*, 169, 156–173.
- Schwartz, M. D., Ault, T. R., & Betancourt, J. L. (2013). Spring onset variations and trends in the continental United States: Past and regional assessment using temperature-based indices. *International Journal of Climatology*, 33, 2917–2922.
- Sugiura, K., Nagai, S., Nakai, T., & Suzuki, R. (2013). Application of time-lapse digital imagery for ground-truth verification of satellite indices in the boreal forests of Alaska. *Polar Science*, 7, 149–161.
- Suzuki, R., Kobayashi, H., Delbart, N., Asanuma, J., & Hiyama, T. (2011). NDVI responses to the forest canopy and floor from spring to summer observed by airborne spectrometer in eastern Siberia. *Remote Sensing of Environment*, 115, 3615–3624.
- Ueyama, M., Iwata, H., & Harazono, Y. (2014). Autumn warming reduces the CO₂ sink of a black spruce forest in interior Alaska based on a nine-year eddy covariance measurement. *Global Change Biology*, 20, 1161–1173.
- Verbyla, D. (2008). The greening and browning of Alaska based on 1982–2003 satellite data. *Global Ecology and Biogeography*, 17, 547–555.
- Vermote, E., & Vermeulen, A. (1999). *Atmospheric Correction Algorithm: Spectral Reflectances (MOD09)* http://modis.gsfc.nasa.gov/data/atbd/atbd_mod09/pdf
- White, M. A., de Beurs, K. M., Didan, K., Inouye, D. W., Richardson, A. D., Jensen, O. P., ... Lauenroth, W. K. (2009). Intercomparison, interpretation, and assessment of spring phenology in North America estimated from remote sensing for 1982–2006. *Global Change Biology*, 15, 2335–2359.
- White, M. A., Thornton, P. E., & Running, S. W. (1997). A continental phenology model for monitoring vegetation responses to interannual climatic variability. *Global Biogeochemical Cycles*, 11, 217–234.
- Widowski, J. L., Pinty, B., Clerici, M., Dai, Y., De Kauwe, M., de Ridder, K., ... Yuan, H. (2011). RAMI4PILPS: An intercomparison of formulations for the partitioning of solar radiation in land surface models. *Journal of Geophysical Research-Biogeosciences*, 116, 25.
- Widowski, J. L., Pinty, B., Lopatka, M., Atzberger, C., Buzica, D., Chelle, M., ... Xie, D. (2013). The fourth radiation transfer model intercomparison (RAMI-IV): Proficiency testing of canopy reflectance models with ISO-13528. *Journal of Geophysical Research-Atmospheres*, 118, 6869–6890.
- Woebbecke, D. M., Meyer, G. E., Vonbargen, K., & Mortensen, D. A. (1995). Color indexes for weed identification under various soil, residue, and lighting conditions. *Transactions of the Asae*, 38, 259–269.
- Xu, L., Myneni, R. B., Chapin, F. S., III, Callaghan, T. V., Pinzon, J. E., Tucker, C. J., ... Stroeve, J. C. (2013). Temperature and vegetation seasonality diminishment over northern lands. *Nature Climate Change*, 3, 581–586.
- Yang, W., Kobayashi, H., Suzuki, R., & Nasahara, K. N. (2014). A simple method for retrieving Understory NDVI in sparse needleleaf forests in Alaska using MODIS BRDF data. *Remote Sensing*, 6, 11936–11955.
- Zhang, X. Y., Friedl, M. A., Schaaf, C. B., Strahler, A. H., Hodges, J. C. F., Gao, F., ... Huete, A. (2003). Monitoring vegetation phenology using MODIS. *Remote Sensing of Environment*, 84, 471–475.
- Zhu, W. Q., Tian, H. Q., Xu, X. F., Pan, Y. Z., Chen, G. S., & Lin, W. P. (2012). Extension of the growing season due to delayed autumn over mid and high latitudes in North America during 1982–2006. *Global Ecology and Biogeography*, 21, 260–271.
- Zona, D., Oechel, W. C., Kochendorfer, J., Paw, U. K. T., Salyuk, A. N., Olivas, P. C., ... Lipson, D. A. (2009). Methane fluxes during the initiation of a large-scale water table manipulation experiment in the Alaskan Arctic tundra. *Global Biogeochemical Cycles*, 23.